Nonlinear motion of optically torqued nanorods

W. Andrew Shelton and Keith D. Bonin*
Department of Physics, Wake Forest University, Winston-Salem, North Carolina 27109, USA

Thad G. Walker
Department of Physics, University of Wisconsin, Madison, Wisconsin 53706, USA
(Received 14 August 2004; published 11 March 2005)

We apply light torques to single optically trapped glass nanorods suspended in water. The resulting motion is studied experimentally and consists of two distinct regimes: a linear regime where the rod angle increases linearly with time and a nonlinear regime where the rod angle changes nonlinearly, experiencing accelerations and rapid reversals. We present a detailed theoretical treatment for the motion of such nanorods, which agrees extremely well with the observed motion. The experiments are carried out so that the trapped and torqued nanorods move without influence from surfaces. Such a model system is critical to understanding the more complex motion that occurs near a surface. Studying such nonlinear motion both free of, and near, a surface is important for understanding nanofluidics and hydrodynamic motion at the nanoscale.

DOI: 10.1103/PhysRevE.71.036204 PACS number(s): 05.45.−a, 87.80.Cc, 83.60.Wc

I. INTRODUCTION

A major success of modern optics has been the application of light forces to microscopic and nanoscopic particles [1]. Recent efforts have also been concentrated on applying light torques at the micro- and nanoscale in optical traps [2–12]. Several of these techniques use optical birefringence and polarized light to exert torques [5,6,10], while others use shape birefringence of asymmetric particles and linearly polarized light to exert torques [2,11,12]. Torques can also be applied with electromagnetic radiation other than light [13]. We also note that an early paper on optically trapped tobacco mosaic virus (TMV) [14] suggested that the TMV nanorods experienced an optical torque in the trap, and oriented parallel to the electric field.

Many of these optical torque papers ignore surface effects. However, it is obvious and interesting that the influence of a surface is important in understanding the motion of objects experiencing an optical torque. Recent research on optical torques on micro- and nanoscale objects has revealed that the motion is very complex. For example, in our earlier work on optically torqued nanorods, novel rocking and chirped motions were observed for motion near a surface [2]. This motion is still not completely understood. Motion of wax microdisks torqued in a linearly polarized optical trap exhibited dynamic Hopf bifurcation, and resulted in periodic oscillation when brought near a wall [11]. There is even disagreement in the literature about whether a flat disk can be torqued by applying linearly polarized trapping light [10,12].

In this work, we apply light torques to asymmetric nanorods using a light-polarization optical trap [2]. Here we used a single beam trap, with light focused through the objective of a standard brightfield microscope, to study the motion of dielectric nanorods under optical torques. In our previous experiments, the optical trapping and torquing laser power was limited to 20 mW, and we could not escape the effects of a nearby surface. To understand the complex influence of surfaces on the motion of nanoparticles, one first has to clearly understand the motion of the particles when they are completely free of the surface. In this work, we have developed a method that frees us of surface effects. The resulting motion is nonlinear, and can be understood using equations of motion that are nonlinear, yet simple to solve in a point-dipole approximation. The results presented here incorporate a range of motions, including behavior near and beyond a saddle-node bifurcation [15]. The observed motion agrees well with our model. This model, of an asymmetric, induced point dipole, under the influence of an optical torque is similar to a driven, damped pendulum in the high damping limit [16]. This model applies to other interesting systems, such as cooperative flashing by a colony of fireflies [17–20], to the firing and propagation of a signal pulse down a neuron [19], and to the phase difference across a Josephson junction [20].

In the next section we discuss the experiment; afterward we review our model of the motion under the conditions of the experiment. Next we present experimental observations and results. Then we analyze the results and compare the observed motion with the theoretical model. At the end, we present some final conclusions.

II. EXPERIMENTAL SETUP

The basic optical setup consisted of an optical tweezers apparatus that used linearly polarized light from an Ar^+ laser; see Fig. 1. Cylindrical borosilicate glass rods of average diameter $d=500$ nm and lengths of $1-5$ μm were optically trapped and torqued. The glass nanorods were suspended in water between two microscope cover slips. The nanorods were held transversely in the optical trap, in the middle of the microscope slide sample, by laser light at wavelength $\lambda=514$ nm focused through a $100\times$, NA$=1.25$ infinity-corrected objective. Light polarization was controlled by adjusting the angle of a half-waveplate relative to the light's

*Electronic address: bonin@wfu.edu

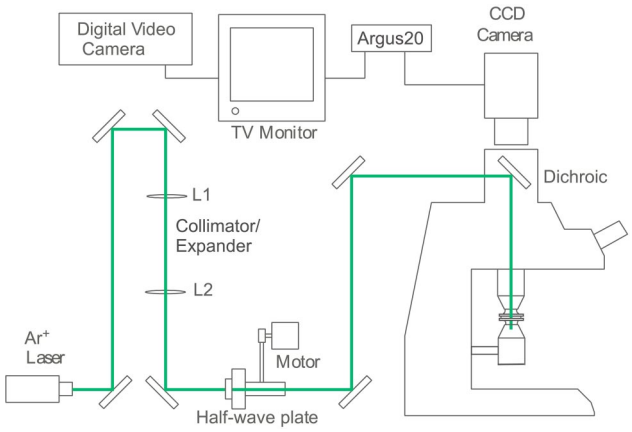

FIG. 1. (Color online) Diagram of the optical layout of the optical tweezers. Rotation of the linearly polarized light by rotation of a half-wave plate applies a torque to the nanorods in the sample between the two objectives.

original polarization axis. The half-waveplate rotates the polarization direction of transmitted light by twice the angle of rotation.

In our previous apparatus [2], we used an Ar^+ laser that was limited to single-beam trapping powers of 20 mW. In such a trap, we observed that if the trapped nanorods were lifted off the microscope slide surface by a distance greater than or about equal to their length, the rods would orient themselves axially in the trap. This means that the rods would have their long axis along the laser beam propagation axis; see Fig. 2. This longitudinal orientation is energetically favorable. To carry out our previous experiments, the rods were kept quite close to the surface in order for the surface to prevent them from orienting axially.

A rod in a beam with infinite waist will orient along the electric field direction. This is confirmed by the early Ashkin work on TMV rods [14], which indicates that smaller rods (300 nm long) will orient along the field in a diffraction-limited beam waist spot. This evidence suggests that by increasing the beam waist, it will be less energetically favorable for a rod to be oriented vertically. Hence, to circumvent our previous restriction of trapping the rods near a surface, we increased the beam waist at trap focus from the nominal minimum of 200 nm, to a value significantly larger. This was achieved by collimating the laser beam to a beam waist of 0.650 ± 0.015 mm at the entrance aperture of the trapping objective. This value was determined by fitting a Gaussian

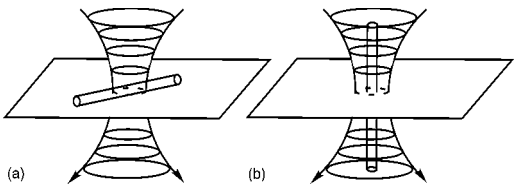

FIG. 2. A sketch of the orientations possible for nanorods described here. The nanorods are trapped in a focused Gaussian beam propagating down. In (a), the nanorod is transversely oriented with respect to the light propagation axis. In (b), the nanorod is axially oriented.

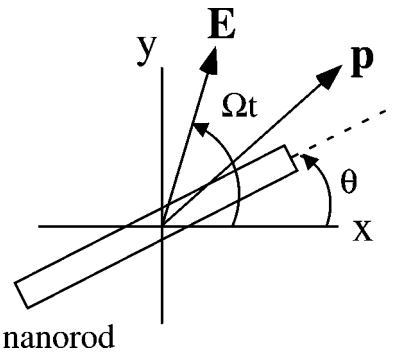

FIG. 3. A sketch of the light torque geometry. Here the induced dipole **p** will move to align with the electric field **E** to minimize energy. Hence, a torque $\boldsymbol{\tau}=\mathbf{p}\times\mathbf{E}$ exists about an axis out of the plane of the paper. The light propagation direction is into the paper.

function to the beam profile measured using a CCD camera placed at the location of the objective's entrance aperture. Neutral density filters were used to reduce beam irradiance to below the saturation level of the camera. The objective's entrance aperture diameter is 8 mm. By significantly underfilling the objective's aperture, the beam waist at the focus is correspondingly increased. We estimate, from the waist measured at the entrance aperture, that the beam waist at trap focus was 0.554 μm. This can be compared to the diffraction-limited case, where a beam waist at the objective entrance of $D_{entrance}/4=2$ mm would produce a waist at the trap focus of 0.2 μm [21]. The latter number is what is expected for an objective of NA=1.25 (like ours) and is the result of diffraction theory, so it is somewhat smaller ($\simeq 85\%$) than the Rayleigh criterion result. Since increasing the trapping focal waist decreases intensity, we used a more powerful Ar^+ laser than in the previous experiments, and we used one capable of delivering up to 500 mW of power at 514 nm. This method succeeded in trapping and torquing nanorods well away from the glass slide and coverslip surfaces.

III. THEORY OF THE MOTION

The basic optical setup consists of an optical tweezers apparatus that uses linearly polarized light. A sketch of a nanorod in such a light field in the trapping plane is given in Fig. 3. Nearly all previous light-driven torquing experiments [3–5,7–9,12,22], involving micron-sized objects, can be understood with ray optics. In contrast, here the important particle dimension d is as small as half the wavelength of light, in the regime between Rayleigh ($d \ll \lambda$) and ray optics ($d \gg \lambda$). Since $d \lesssim \lambda$, and since we plan to investigate even smaller spatial regimes, we discuss the basic light-particle interaction in the Rayleigh limit. We assume the trapped particle is a homogeneous, asymmetric, nonabsorbing dielectric object immersed in a dielectric liquid. The linearly polarized electric field of the laser beam **E** induces a dipole moment $\mathbf{p}=\vec{\alpha}\cdot\mathbf{E}$, where $\vec{\alpha}$ is the polarizability tensor of the nanoparticle. The light field applied to an asymmetrically shaped particle induces a dipole moment that is not parallel to the inducing electric field.

To minimize energy, the induced dipole moment **p** wants to align with the field; see Fig. 3. The optical torque, given by $\boldsymbol{\tau}=\mathbf{p}\times\mathbf{E}$, is proportional to the polarizability difference $\Delta\alpha=\alpha_{\parallel}-\alpha_{\perp}$, where $\alpha_{\parallel}$, $\alpha_{\perp}$ are the polarizability components parallel and perpendicular to the long axis of the rod. In the Appendix, we briefly derive the relation between the torque and the polarizability anisotropy $\Delta\alpha$ in the Rayleigh particle regime.

The other torque acting on the nanorods (when they are moving) is that due to Stokes drag by the medium (water). From Newton's second law, we can write the basic equation of motion as

$$I\frac{d^2}{dt^2}\theta = N\sin[2(\Omega t-\theta)] - \gamma\frac{d}{dt}\theta. \tag{1}$$

Here I is the moment of inertia of the nanorod; θ is the angle of the nanorod axis with respect to a fixed laboratory frame axis; $N=-\Delta\alpha E_0^2/4$ is the torque amplitude (time-averaged over one optical cycle, see the Appendix); Ω is the angular rotation frequency of the light polarization axis; and γ is the angular drag coefficient from Stokes law for rotation in a viscous medium [23]. The quantity E_0^2 is the squared magnitude of the electric field at the location of the trap.

The equation of motion can be put into dimensionless form with the following changes: introduce the parameter $\Omega_c=N/\gamma$, define $u=2\Omega_c t$, go to a corotating frame (rotating with the angular frequency of the rotating electric field polarization, Ω), and define $\phi=2(\Omega t-\theta)$. With a little algebra, we can then write Eq. (1) as

$$\frac{2I\Omega_c}{\gamma}\ddot{\phi}+\dot{\phi}=\frac{\Omega}{\Omega_c}-\sin\phi, \tag{2}$$

where each overdot indicates a derivative with respect to u, i.e., d/du. Under our experimental conditions, where the moment of inertia of the object is extremely small, the first term on the left hand side (the inertial term) is entirely negligible. For example, typical experimental values for the coefficients in this term are $I=3\times10^{-28}$ kg m^2 (glass nanorod length of 3800 nm, radius of 250 nm), $\Omega_c=30$ rad/s, and $\gamma=3.8\times10^{-20}$ kg m^2/s. These values make the coefficient small, e.g., $2I\Omega_c/\gamma\approx4\times10^{-7}$. For comparison, $\Omega/\Omega_c\approx0.1-10$. Hence, the inertial term in Eq. (2) can be neglected in our analysis.

We now consider solutions to the equation of motion, which has the form

$$\dot{\phi}=\frac{\Omega}{\Omega_c}-\sin\phi. \tag{3}$$

This is a nonlinear first-order differential equation describing the angular motion of the nanorods in a rotating frame. Equation (3), which is very close to the model of a driven, damped, simple pendulum when the damping dominates the inertia, has been discussed in the literature [15] and in textbooks [20]. Actually, Eq. (3) is a model for the synchronization of the flashing of fireflies [17,18] and for the phase difference in the flow of current in a Josephson junction [20]. The character of the solution to Eq. (3) differs depending on whether the driving frequency Ω is below or above the "critical" frequency Ω_c. In the case where Ω is below Ω_c ($\Omega/\Omega_c<1$), there are two solutions, one stable and one unstable. The stable solution is for $\dot{\phi}=0$, and $\phi=\arcsin(\Omega/\Omega_c)$. In the laboratory frame, where the nanorod angle $\theta=\Omega t-\phi/2$, the nanorod angle θ rotates at the same rate as the laser polarization, Ω, but lags in phase by $\phi/2$. Physically, the rod continuously and smoothly rotates at the same rate as the laser polarization, i.e., its rotation is *phase-locked* to the polarization rotation. As the polarization rotation rate increases, then $\Omega_c/\Omega\to1$. Here, the stable and unstable points converge to form a saddle-node bifurcation [15]. Physically, the polarization rotation rate equals the critical frequency, i.e., $\Omega=\Omega_c$.

In the second case, where Ω is above Ω_c ($\Omega/\Omega_c>1$), Eq. (3) shows that $\dot{\phi}>0$, which means the solution is periodic and exhibits a limit cycle in phase space ($\dot{\phi}$ versus ϕ). In the physical, laboratory frame, $\dot{\phi}>0$ means that $\Omega t>\theta$ and so the laser polarization rotates more rapidly than the nanorod. Physically, this will cause the laser polarization to move far enough ahead of θ to flip the direction of torque, which will cause the nanorod angular velocity to decrease and become negative. Hence the nanorod will rotate in a direction opposite to its original direction, i.e., it will 'flip back." This cycle, of increasing angle with time, punctuated by "flip-backs," where the angle decreases with time, continues without change as long as experimental conditions remain the same.

IV. RESULTS

The data consisted of a stream of video images that could be analyzed after the experiment ended. Figure 4 shows a montage of images corresponding to the motion of a 3.8-μm-long nanorod being driven at a laser polarization frequency that is below the critical frequency, i.e., $\Omega<\Omega_c$. This nanorod was 24 μm above the bottom surface of the sample and about 7 μm from the nearest top surface. Hence it was more than 20 radii away from the closest surface, and surface effects are negligible.

Figure 5 shows a sequence of images that corresponds to the motion when the laser polarization rotation frequency exceeds the critical frequency, i.e., $\Omega>\Omega_c$. This sequence is a small set of a much larger set of 160 images that recorded the motion under the same conditions.

V. ANALYSIS AND DISCUSSION

The results (sequences of images for a given laser polarization rotation rate Ω) were analyzed frame-by-frame using an angle tool in an imaging software program. This tool was used to determine the angle of the rod in each image with respect to the horizontal x axis. This angle corresponds to θ in Fig. 3. The time difference between two adjacent images was about 33 ms, since the frame rate of the camera was 29.97 Hz (RS-170 standard). Hence the data extracted from each frame of a given set of images (fixed Ω) were the time, t, and the rod orientation angle, θ, at that time. Tables of the resulting time-angle pairs (t,θ) were then used to plot the

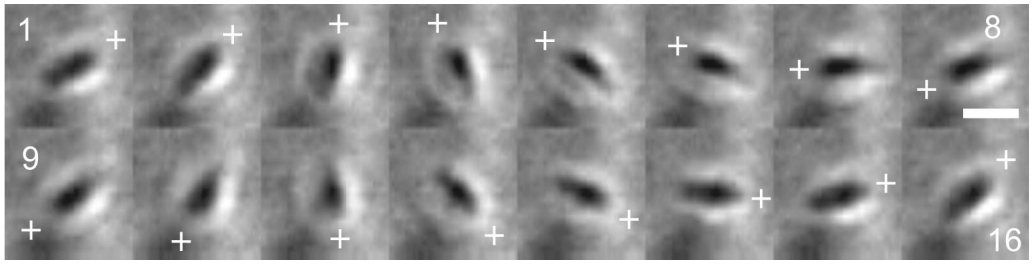

FIG. 4. A sequence of images showing the motion of a nanorod under the influence of the light torque with a phase-locked response, i.e., the rod keeps a fixed phase difference with respect to the rotating polarization of the light. The motion is counterclockwise from left to right, as indicated by the crosses (+) that follow one end of the nanorod for all 16 images. We show one complete period and in this case the angular polarization rotation rate was $\Omega = 2\pi \times 2$ Hz. Scale bar corresponds to 4 μm.

time-dependent evolution of the laboratory orientation of the nanorods under the influence of the optical torque. Here we present plots of the motion of the rod, θ versus t, for the two different classes of the motion: (i) linear, phase-locked motion, where $\Omega < \Omega_c$, and (ii) nonlinear motion, where $\Omega > \Omega_c$.

Case 1: Phase-locked motion ($\Omega < \Omega_c$). In Fig. 6, we have plotted the rod angle versus time, θ versus t, under the condition where $\Omega = 2\pi \times 4.06$ Hz and $\Omega_c \simeq 2\pi \times 4.8$ Hz ($\Omega < \Omega_c$). The method used to deduce a value for the critical frequency Ω_c is given below. The solid line in Fig. 6 represents the best linear fit to the data. This line exactly coincides with the line corresponding to the electric field polarization angle versus time (Ωt versus t), which has a slope of $\Omega = 2\pi \times 4.06$ Hz, compared to the best-fit slope of $2\pi \times 4.057$ Hz. Since the two slopes agree to better than a part in 2000, it is clear that the rod's motion follows the rotation of the electric field polarization with high fidelity. Data at other values of $\Omega < \Omega_c$ agreed equally well with the model in each case.

Case 2: Nonlinear motion ($\Omega > \Omega_c$). In Fig. 7, we have plotted the rod angle versus time, θ versus t, under the condition where $\Omega = 2\pi \times 5$ Hz and $\Omega_c \simeq 2\pi \times 4.8$ Hz ($\Omega > \Omega_c$). The solid line represents the electric field polarization angle versus time (Ωt versus t). Notice that the rod motion here differs in two key ways compared to the first case. First, the average slope of the rod angle is significantly lower than the slope of the electric field polarization angle. Second, note that there are repeating occurrences of regions where the slope of the rod angle becomes negative. These regions where the rod angle decreases are labeled "flipbacks." During a flipback, the rod momentarily reverses direction. The motion appears basically "linear," and the amplitude and frequency of the flipbacks change with time. There are shorter sections of the data in which the flipbacks are periodic, as discussed below. However, for conditions near the critical frequency, the periodicity of the flipback regions is irregular over long times, for reasons that will be described shortly. When the laser polarization frequency is well above the critical frequency, flipbacks are more periodic and more frequent, resulting in an even lower θ versus t slope.

Note that both regions of motion are solutions to the nonlinear equation of motion Eq. (3). However, we classify the motion as linear or nonlinear using the following rule: *linear* motion refers to the motion where the angle of the rod changes (increases or decreases) *linearly* with time; *nonlinear* motion refers to the motion where the angle of the rod changes nonlinearly with time.

A. Specific case: $\Omega \gtrsim \Omega_c$

To better understand the motion, to compare our observations to theory, and to estimate a value of Ω_c, we consider a short part of the motion in the nonlinear case [case (2) above]. We study data where Ω is close to the critical frequency Ω_c. In Fig. 8, we have selected out the rod angle versus time points from Fig. 7 for the region $2.5\ \text{s} < t < 3.7$ s. These data have been shifted so their origin is at time $t = 0$ in Fig. 8. The solid line in Fig. 8 corresponds to the best fit of the solution to Eq. (3) to the data in this region. In the fit, three parameters were varied: the angular polarization rotation rate (Ω), the critical frequency (Ω_c), and a constant

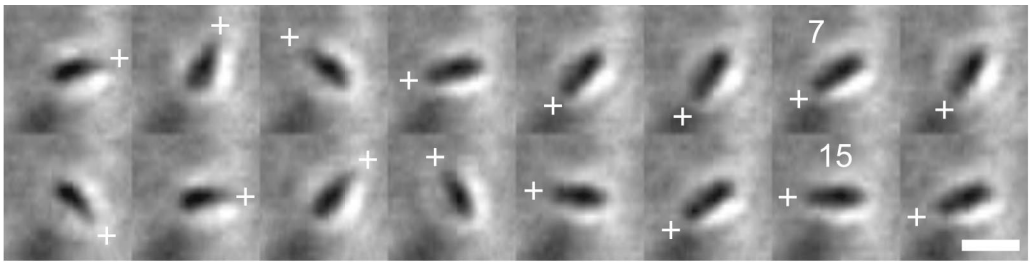

FIG. 5. A sequence of images showing the motion of a nanorod under the influence of the light torque with a nonphased response, i.e., the rod is not moving in phase with the rotating polarization of the light. The motion is counterclockwise from left to right, as indicated by the crosses (+) that follow one end of the nanorod for all 16 images. It is clear that the nanorod periodically reverses direction, as in frames 7 and 15 here. The angular polarization rotation rate was $\Omega = 2\pi \times 5$ Hz. Scale bar corresponds to 4 μm.

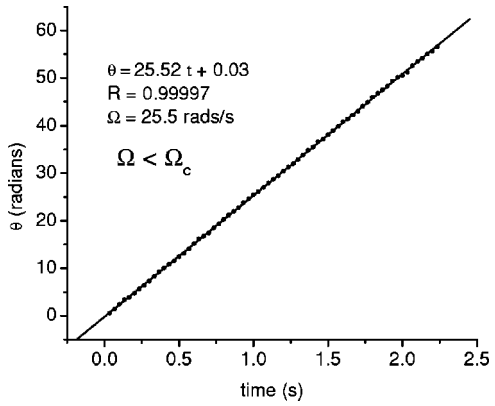

FIG. 6. A plot of the nanorod orientation θ as a function of time t for linear motion. Here $\Omega=2\pi\times4.06$ Hz and $\Omega_c\simeq2\pi\times4.8$ Hz, so $\Omega<\Omega_c$. The solid line represents the best linear fit to the data.

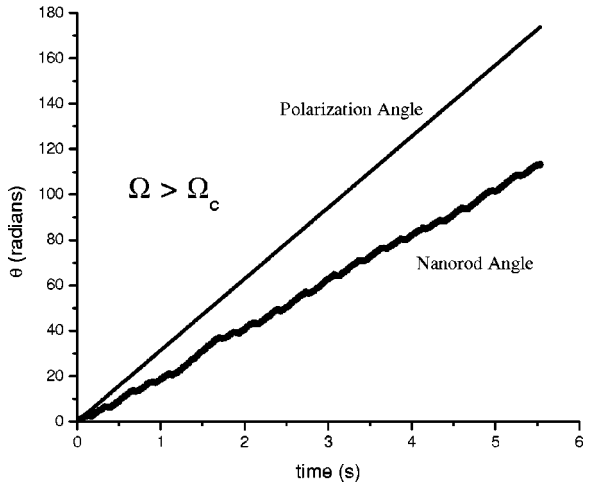

FIG. 7. A plot of the nanorod orientation θ as a function of time t for nonlinear motion. In addition, we have plotted the laser polarization rotation angle Ωt during the same time. This corresponds to the case where $\Omega=2\pi\times5$ Hz and $\Omega_c\simeq2\pi\times4.8$ Hz.

phase β, i.e., $\phi=2(\Omega t-\theta)+\beta$ in Eq. (3). The fit was done using a nonlinear least-squares Marquardt-Levenberg technique in MATLAB using the ode45 differential equation function to numerically solve the nonlinear differential equation Eq. (3) each time. The final values for the fitting parameters were $\Omega=2\pi\times5.14$ Hz, $\Omega_c=2\pi\times4.90$ Hz, and $\beta=1.65$ radians. For these data, the electric field polarization rotation rate was set to $2\pi\times5$ Hz, according to the setting on the pulse generator driving the stepper motor that determines the rotation rate of the half-waveplate. Hence the fitted value for this parameter of $\Omega=2\pi\times5.14$ Hz is within 3% of the value expected by the setting on the motor driving the half-waveplate. It appears that the theory fits the data rather well for appropriate values of the parameters. Hence, in both the linear and nonlinear motion regimes, the model summarized by Eq. (3) does an excellent job.

We have now provided enough analysis of the data to discuss the motion in Fig. 7 in complete detail. As already mentioned, there are sections where the motion is periodic, sections that have irregular or changing periods, and there is even a region that is linear (in the time range $1.2\text{ s}<t<1.7$ s). Note that this linear region has a slope identical to the slope of the laser polarization angle line. These irregularities in the period of the nonlinear motion [characterized by solutions to Eq. (3)] and the linear motion region present on the same curve indicate that the critical frequency, or the laser polarization frequency, change during a data run. For example, a changing critical frequency could explain the data plotted in Fig. 7. For most of the data, the motion is nonlinear and $\Omega>\Omega_c$. However, for the linear motion in the time range $1.2\text{ s}<t<1.7$ s, the critical frequency could have risen above the laser polarization frequency Ω to produce the phase-locked motion typical of the linear motion regime. Thus, we need to discuss the experimental conditions that could lead to changes in Ω or Ω_c during a data run.

First, we consider possible changes in the laser polarization frequency Ω. Changes in Ω can occur due to stepper motor variations in rotation rate. The stepper motor that rotates the half-wave plate is driven by square pulses from a frequency generator. These pulses are periodic to better than 1%. However, all motors, including the one used here, have resonant frequencies at which the motor body vibrates significantly, and mechanical noise is coupled into the table or mount that holds the stepper motor. A key indicator that the motor-half-waveplate system worked very periodically in our setup is the data in the linear regime; see Fig. 6. Here the data show a very linear θ versus t motion response, which could only result if the motion of the motor-half-waveplate system is very linear. However, note that the motor response differs at different frequencies.

Second, we consider possible changes in the critical frequency Ω_c. Changes in $\Omega_c=N/\gamma$ can occur due to changes in the torque amplitude N or drag coefficient γ. It is unlikely that the drag coefficient changes during a run, since it depends on very stable physical parameters: rod length, rod diameter, and fluid viscosity. In contrast, it is almost assured that the torque amplitude $N=-\Delta\alpha E_0^2/4$ changes under the conditions of the experiment. The irradiance of the laser can vary due to thermal drift, pointing direction drift, or variations, or due to variations in the power supply electronics driving the laser plasma tube. These variations are estimated to be less than 3% during the time of our experiments (about 2–3 h). Two optical elements in our experiment also gave rise to variations in laser irradiance delivered to the nano-

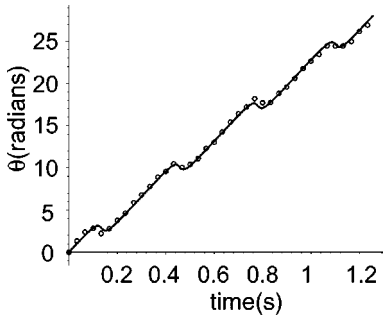

FIG. 8. A plot of the nanorod orientation θ as a function of time t. The solid curve corresponds to a nonlinear least-squares fit to the data. The final values for the fitting parameters were $\Omega=2\pi\times5.14$ Hz, $\Omega_c=2\pi\times4.90$ Hz, and $\beta=1.65$ (see text for details).

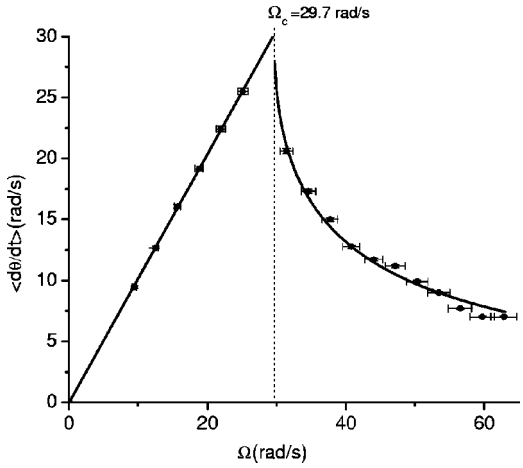

FIG. 9. Plot of the average nanorod rotation rate $\langle d\theta/dt\rangle$ versus the laser-polarization-rotation rate Ω. For values of $\Omega<\Omega_c$, the dependence is linear. For $\Omega>\Omega_c$, the rod rotation rate declines monotonically as Ω is increased. In both regions, the solid curves represent the fitted function; for $\Omega<\Omega_c$, the function is linear and for $\Omega>\Omega_c$, the fitted function is given in Eq. (4). Vertical error bars are about 1% of the *y* values, while the horizontal error bars are 3% of *x* values.

rods. The half-waveplate would vary the irradiance at the sample by ±2.5%. This value was determined by measuring the laser power transmitted through the microscope objective with an accurate power meter. The transmitted power, measured as a function of the half-waveplate angle, systematically varied by 5%. Another optical element present in the experiment, but not shown in Fig. 1, was a nonpolarizing beamsplitter. Placed just after the half-waveplate, it was used for monitoring and alignment purposes. The measured variation in laser power as a function of laser polarization angle was also 5% (±2.5%). The variations in laser power, and hence critical frequency Ω_c, could easily explain the variation in the periodic motion under nonlinear motion conditions, or under conditions near the critical frequency. We reiterate that, at laser polarization frequencies well above the critical frequency, straight sections whose slope equals Ω do not occur, and the motion has periodic and more frequent flipbacks that significantly reduce the slope of the θ versus t data.

Finally, we mention another way to determine the critical frequency under the existing experimental conditions. It requires analyzing data over the whole range of laser-polarization-rotation frequencies Ω. Below the critical frequency, the rod rotation frequency follows the driving, laser-polarization-rotation frequency and so $d\theta/dt=\Omega$ $(\Omega<\Omega_c)$. However, when $\Omega>\Omega_c$, then $d\theta/dt$ is not constant, but the average frequency $\langle d\theta/dt\rangle$ can be determined from a linear fit to the θ versus t data. Then curves like Figs. 6 and 7 can be summarized in a plot of $\langle d\theta/dt\rangle$ versus Ω over the whole range of laser-polarization-rotation frequencies. The resulting curve of $\langle d\theta/dt\rangle$ versus Ω is given in Fig. 9. It can be shown that for $\Omega>\Omega_c$

$$\left\langle \frac{d\theta}{dt} \right\rangle = \Omega - \sqrt{\Omega^2 - \Omega_c^2}. \tag{4}$$

The solid curve in Fig. 9 in the region $\Omega>\Omega_c$ corresponds to Eq. (4). For $\Omega<\Omega_c$, the slope is unity. By fitting the whole range of data to these two functions, Ω_c can be determined. In this case we obtain a value slightly lower, $\Omega_c=2\pi\times4.73$ Hz, than the Ω_c determined by fitting the data in Fig. 8, where $\Omega_c=2\pi\times4.90$ Hz.

B. Effect of Brownian motion

It is important to discuss how Brownian motion would affect the observations and results presented here. Brownian motion refers to the random motion of a particle suspended in a medium due to the random collisions of medium particles with the object. To determine whether noise from Brownian motion is important, we need to estimate the change in angle due to Brownian motion during the time it takes to record one image (1/30 s). For a one-dimensional random walk, the mean-square angle of rotation during a time t is [23]

$$\langle \theta^2 \rangle = 2D_r t, \tag{5}$$

where the rotational diffusion constant D_r is

$$D_r = \frac{kT}{\gamma}. \tag{6}$$

Here k is Boltzmann's constant, T is the temperature, and γ is the rotational drag coefficient, identical to the term found in Eq. (1). For a rod of length L and radius r, the rotational drag coefficient is

$$\gamma = \frac{\pi\eta}{3}\frac{L^3}{\ln\left(\frac{L}{2r}\right) - 0.66}, \tag{7}$$

where η is the viscosity of the surrounding medium. Using the usual numbers for viscosity of water, and the dimensions for the rod here ($L=3.8$ μm and radius=250 nm), we find $\gamma=3.7\times10^{-13}$ g cm^2/s, and that $D_r=0.11$ rad^2/s. Hence, during the time it takes to record one image (integration time of a frame, 33 ms), the rod has an rms rotation of $\sqrt{\langle\theta^2\rangle}=0.085$ radians/frame. For comparison, close to the critical frequency the rod rotation rate due to the optical torque is about 30 rad/s, which is about 1 radian each frame. Hence, rotation due to the light torque is a factor of 12 higher than the corresponding rotation due to Brownian motion during a given time interval. For perspective, note that the size of a data point symbol in Fig. 6 (solid circles) corresponds to an angle of 0.85 radians. This is 10 times larger than the noise due to Brownian motion during the time of a single frame for such a data point. Hence the Brownian noise contributes in a small way to the overall noise displayed in the figures.

As a final note, we briefly mention the importance of using longer nanorods to observe the linear and nonlinear behavior (linear below, and nonlinear above, the critical frequency Ω_c). In fact, smaller rods remained in the region below the saddle node in all the small rod cases we tried

(generally their length was 1 μm or less). Hence, smaller rods did not exhibit the transition through the saddle node bifurcation. The reason for this is that longer rods have a much higher rotational drag coefficient γ since $\gamma \propto L^3$, where L is the rod length, see Eq. (7). For larger rods, this has the effect of lowering the critical frequency into an experimental range where the saddle node bifurcation can be observed. This also has the advantage of helping decrease Brownian rotation, since the diffusion constant depends inversely on drag coefficient γ. Also the data analysis is easier with a larger object. We could also have lowered the torque amplitude N to get into a range where the transition behavior was apparent. However, this has the deleterious effect of also lowering the trapping depth, which would make the relative importance of Brownian motion greater. In addition, γ could have been increased by increasing the viscosity of the medium. For example, a 50% glycerin-water mixture would increase the viscosity a factor of 2.5. However, the optical properties of the sample would change and the trapping depth would have been lowered. Finally, the polarization rotation rate Ω could also be used to put the motion into the range to see the transition behavior. This would have required using a different motor or different gearing to increase or decrease the rotation rate.

VI. CONCLUSIONS

We have presented detailed experimental results on the nonlinear motion of glass nanorods optically torqued by rotating linearly polarized light. The experiments were conducted far from surfaces, making the results extremely useful for understanding the basic physics of optically torqued nanorods. We have also provided an approximate point-dipole model for the optically torqued nanorods that gives good agreement with experimental results. Our observations, and the nonlinear equations of motion, show that there are two distinct types of motion: phase-locked rotation and flipback motion. For driving frequencies beyond the critical frequency, the motion exhibits nonlinear, flipback oscillations. This model system will serve as a benchmark for understanding the motion in more complex regimes, such as motion near surfaces. Already, work on optically trapped disks has provided some valuable insights into the rheological behavior of polymer solutions at the nanoscale [24].

ACKNOWLEDGMENTS

We thank the Johns-Manville Corporation for providing glass fibers. W.A.S. thanks Wake Forest University for their support; T.G.W. was partially supported by the NSF. We thank C.W. Yip for his help in using imaging software. We also thank Robert Morris for technical assistance, Robert Swofford and Jeff Weiner for the loan of critical equipment, and George Holzwarth for labspace and the use of his equipment.

APPENDIX

In this appendix, we derive an expression for the light torque on an induced point dipole; see Fig. 3. Consider the simple case of an applied electric field that is a plane wave of the form

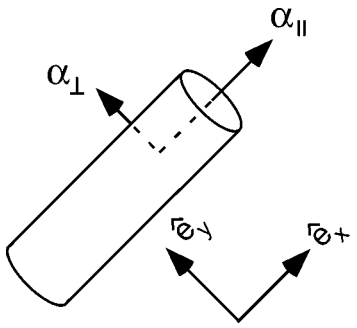

FIG. 10. Sketch showing the tensor components in the body frame of the rod.

$$\mathbf{E}(\mathbf{r},t) = \frac{1}{2}[\mathbf{E}_0(\mathbf{r})e^{-i\omega t} + \text{c.c.}], \tag{A1}$$

where the symbol c.c. refers to the complex conjugate of the term that came before it. The electric dipole induced by this field can then be written

$$\mathbf{p}(\mathbf{r},t) = \frac{1}{2}[\mathbf{p}_0(\mathbf{r})e^{-i\omega t} + \text{c.c.}]. \tag{A2}$$

The amplitude $\mathbf{p}_0(\mathbf{r})$ of the oscillating dipole is given by

$$\mathbf{p}_0(\mathbf{r}) = \overleftrightarrow{\alpha} \cdot \mathbf{E}_0(\mathbf{r}), \tag{A3}$$

where $\overleftrightarrow{\alpha}$ is the polarizability tensor. A tensor description of the polarizability is important because the torque on our particles arises from the property of shape birefringence. Asymmetrically shaped particles, such as rods, disks, and ellipsoids, have differing polarizabilities along the principal axes. For details on shape birefringence, consult an advanced text on classical electrodynamics or light scattering [25–27]. It is important to note that the tensor polarizability causes the induced dipole moment to point in a direction that is not along the electric field direction; see Fig. 3. The polarizability tensor can be expressed as a matrix, which becomes diagonal if we consider the optical (body) axes of the glass rod; see Fig. 10. Thus in this appendix the coordinate system will correspond to the body axes given in Fig. 10. For a cylindrical glass rod, we can write the polarizability tensor in this frame as

$$\overleftrightarrow{\alpha} = \begin{bmatrix} \alpha_{\parallel} & 0 & 0 \\ 0 & \alpha_{\perp} & 0 \\ 0 & 0 & \alpha_{\perp} \end{bmatrix}. \tag{A4}$$

The torque on a point dipole in an electric field is given by

$$\boldsymbol{\tau} = \mathbf{p}(t) \times \mathbf{E}(t). \tag{A5}$$

To evaluate Eq. (A5) for our geometry, define the instantaneous angle between the electric field and the point dipole to be $\beta = \Omega t - \theta$ (see Fig. 3). Writing both the field amplitude $\mathbf{E}_0(\mathbf{r})$ and the dipole amplitude $\mathbf{p}_0(\mathbf{r})$ in terms of the body axes of the rod (see Fig. 10), we have

$$\mathbf{E}_0 = E_{0x}\hat{e}_x + E_{0y}\hat{e}_y = E_0(\cos\beta\hat{e}_x + \sin\beta\hat{e}_y) \tag{A6}$$

and

$$\mathbf{p}_0 = \alpha_{xx}E_{0x}\hat{e}_x + \alpha_{yy}E_{0y}\hat{e}_y = \alpha_{\parallel}E_{0x}\hat{e}_x + \alpha_{\perp}E_{0y}\hat{e}_y. \tag{A7}$$

The torque Eq. (A5) is then

$$\mathbf{p}(t)\times\mathbf{E}(t) = \begin{vmatrix} \hat{e}_x & \hat{e}_y & \hat{e}_z \\ \alpha_{\parallel}E_{0x} & \alpha_{\perp}E_{0y} & 0 \\ E_{0x} & E_{0y} & 0 \end{vmatrix} \cos^2\omega t \tag{A8}$$

$$= \hat{e}_z(\cos^2\omega t)E_{0x}E_{0y}(\alpha_{\parallel} - \alpha_{\perp}) \tag{A9}$$

$$= \hat{e}_z E_0^2(\cos^2\omega t)(\alpha_{\parallel} - \alpha_{\perp})\cos\beta\sin\beta. \tag{A10}$$

Since the angle β changes very slowly on an optical time scale, we perform a time average of the torque over one optical cycle, $T = 2\pi/\omega$. This time average, denoted by angular brackets, gives $\langle\cos^2\omega t\rangle = 1/2$. Using this, the trigonometric relation $\cos\beta\sin\beta = (1/2)\sin 2\beta$, and substituting $\beta = \Omega t - \theta$ gives an expression for the time-averaged torque (time-averaged over one optical cycle)

$$\langle\boldsymbol{\tau}\rangle = \frac{1}{4}E_0^2(\alpha_{\parallel} - \alpha_{\perp})\sin[2(\Omega t - \theta)]\hat{e}_z. \tag{A11}$$

This expression is the first term on the right-hand side of Eq. (1).

[1] A. Ashkin, Proc. Natl. Acad. Sci. U.S.A. **94**, 4853 (1997).
[2] K. Bonin, B. Kourmanov, and T. Walker, Opt. Express **10**, 984 (2002).
[3] R. Gauthier, M. Ashman, and C. Grover, Appl. Opt. **38**, 4861 (1999).
[4] E. Higurashi, H. Ukita, H. Tanaka, and O. Ohguchi, Appl. Phys. Lett. **64**, 2209 (1994).
[5] M. Friese, T. Nieminen, N. Heckenberg, and H. Rubinsztein-Dunlop, Nature (London) **394**, 348 (1998).
[6] E. Higurashi, R. Sawada, and T. Ito, Phys. Rev. E **59**, 3676 (1999).
[7] Z.-P. Luo, Y.-L. Sun, and K.-N. An, Appl. Phys. Lett. **76**, 1779 (2000).
[8] P. Galadja and P. Ormos, Appl. Phys. Lett. **78**, 249 (2001).
[9] L. Paterson, M. MacDonald, J. Arlt, W. Sibbett, P. Bryant, and K. Dholakia, Science **292**, 912 (2001).
[10] Z. Cheng, P. Chaikin, and T. Mason, Phys. Rev. Lett. **89**, 108303 (2002).
[11] Z. Cheng, T. Mason, and P. Chaikin, Phys. Rev. E **68**, 051404 (2003).
[12] P. Galagja and P. Ormos, Opt. Express **11**, 446 (2003).
[13] T. Jones, *Electromechanics of Particles* (Cambridge University Press, New York, 1995).
[14] A. Ashkin and J. Dziedzic, Science **235**, 1517 (1987).
[15] M. Argentina, P. Coullet, and L. Mahadevan, Phys. Rev. Lett. **79**, 2803 (1997).
[16] S. Thornton and J. Marion, *Classical Dynamics of Particles and Systems*, 5th ed. (Thomsen/Brooks Cole, Belmont, 2004).
[17] R. Mirollo and S. Strogatz, SIAM J. Appl. Math. **50**, 1645 (1990).
[18] G. B. Ermentrout, J. Math. Biol. **29**, 571 (1991).
[19] Personal communication, H. Riecke, Northwestern University, May 2004. See the elegant and extensive notes at http://www.esam.northwestern.edu/riecke/lit/438notes.pdf
[20] S. Strogatz, *Nonlinear Dynamics and Chaos* (Addison-Wesley, Reading, MA, 1994).
[21] J. Squier and M. Muller, Rev. Sci. Instrum. **72**, 2855 (2001).
[22] E. Higurashi, O. Ohguchi, T. Tamamura, H. Ukita, and R. Sawada, J. Appl. Phys. **82**, 2773 (1997).
[23] M. Tirado and J. de la Torre, J. Chem. Phys. **73**, 1986 (1980).
[24] Z. Cheng and T. Mason, Phys. Rev. Lett. **90**, 018304 (2003).
[25] J. Stratton, *Electromagnetic Theory* (McGraw-Hill, New York, 1941).
[26] H. van de Hulst, *Light Scattering by Small Particles* (Dover, New York, 1981).
[27] L. D. Landau, E. Lifshitz, and L. Pitaevskii, *Electrodynamics of Continuous Media*, 2nd ed. (Pergamon Press, Oxford, 1984).